Molecular packing-dependent photoconductivity in functionalized anthradithiophene crystals

K. Paudel,[a] G. Giesbers, [a] J. Van Schenck, [a] J. E. Anthony,[b] O. Ostroverkhova[a]

[a]*Department of Physics, Oregon State University, Corvallis, OR 97331*

[b]*Department of Chemistry, University of Kentucky, Lexington KY*

Abstract:

We relate features observed in time-resolved photocurrent with crystal structure and disorder in crystals of two anthradithiophene (ADT) derivatives with different packing motifs, diF TES-ADT and diF TSBS-ADT.[1]

A factor of ~10-12 higher peak photocurrent was obtained in the diF TES-ADT crystals characterized by a 2D "brickwork" packing as compared to diF TSBS-ADT with a 1D "sandwich-herringbone" packing, primarily due to differences in intrinsic charge carrier mobility. A change from shallow trap-mediated thermally activated regime at 230-300 K (200-300 K), with a zero-electric field activation energy of ~40-50 meV, in the TES (TSBS) derivative to the temperature independent behavior at lower temperatures in both derivatives was observed. The shallow traps were attributed to structural defects associated, for example, with a solid-solid phase transition in the TES derivative. In diF TES-ADT, most charge trapping in shallow traps occurred on <0.4 ns time scales at all temperatures (80 - 300 K) and the carriers that were mobile at 0.4-10 ns time scales at 300 K remained mobile at 80 K. In contrast, shallow trapping in the diF TSBS-ADT crystals proceeded on the nanosecond time scales, with a pronounced loss of mobile carriers at low temperatures. This was followed by deep trapping at longer time scales, which led to a factor of ~250 lower steady-state photocurrent obtained under continuous wave excitation in the diF TSBS-ADT crystals as compared to diF TES-ADT.

[1] ADT = anthradithiophene; TES = (triethylsilyl)ethynyl; TSBS = tri-sec-butylsilylethynyl

I. Introduction

Organic semiconductors are of interest due to their applications in low-cost, large-area (opto)electronic devices; these include thin-film transistors, solar cells, light-emitting diodes, photodetectors, sensors, and many others.[1] Tremendous progress in device performance has been achieved over the past 10 years due to better understanding of fundamental processes that determine (opto)electronic properties of organic materials, as well as of structure-property relations that led to the development of improved fabrication methods enabling optimized structure and morphology. In spite of the progress, many fundamental questions pertaining to charge carrier dynamics in organic materials, especially crystalline materials, remain.[2–6] These include the mechanisms that contribute to the "bandlike" behavior of charge carrier mobility (typically defined as mobility decreasing as the temperature increases)[1] and quantitative assessment of an interplay between coherent and incoherent charge transport.[6,7] On the molecular design side, several criteria for enhancing charge transport have been outlined that include maximizing the transfer integral, making it as isotropic as possible,[8] minimizing the reorganization energy,[9] increasing the intermolecular vibration frequency,[6] and minimizing the long-axis displacement due to molecular vibrations.[10]

Relative contributions of various aspects of molecular packing to charge carrier mobilities in organic crystals have also been under investigation. For example, highest charge carrier mobilities have been obtained in crystals featuring either "herringbone" (e.g. unsubstituted pentacene (Pn) or rubrene) or two-dimensional (2D) "brickwork" packing (e.g. TIPS-Pn or F2-TCNQ).[1] However, which property enabled by such packing is the dominant factor is still under debate.[11,12] An instructive illustration of effects of molecular packing on electronic properties is obtained by comparison of charge carrier mobilities achieved in different polymorphs of the same material.[13–15] For example, an order of magnitude higher hole mobility was observed in perylene polymorph FETs featuring "herringbone" packing as compared to those with a 1D "sandwich-herringbone" packing due to a stronger, higher-dimensional edge-to-face interactions in the "herringbone" structure.[15] Similarly, more than an order of magnitude higher mobility was observed in single crystal FETs of a functionalized dibenzochrysene derivative with a 2D "brickwork" packing as compared to its polymorph with a 1D "slip-stack" packing.[13] However, in this case similar intrinsic mobilities were expected for both polymorphs based on theoretical predictions, and extrinsic contribution from defects that affect the 1D transport in a more pronounced way than the 2D transport was partially responsible for the observed differences.

In the present study we investigated how molecular packing determines various aspects of photoinduced time-resolved charge carrier dynamics in crystals of two functionalized anthradithiophene (ADT) derivatives, diF TES-ADT (TES = (triethylsilyl)ethynyl) and diF TSBS-ADT (Fig. 1(a)). Functionalized fluorinated ADT derivatives have been extensively studied in field-effect transistors (both in the single-crystal and in the thin-film form)[16–21] and in devices relying on the ADT's strong photoconductive response.[22–27] One of the highest-performing ADT derivatives, diF TES-ADT, exhibited hole mobilities of up to 6 $cm^2/(Vs)$ in single crystals[17] and up to 6.7 $cm^2/(Vs)$ in ultra-thin highly-ordered diF TES-ADT:PS (PS = polystyrene) films.[28] This derivative exhibits the 2D "brickwork" molecular packing, one of the most successful packing motifs for FETs as discussed above. The diF TSBS-ADT (TSBS = tri-sec-butylsilylethynyl) derivative exhibits a drastically different, 1D "sandwich-herringbone" packing motif.[29,30] This derivative

has been previously studied in TFTs; however, TFT mobilities of lower than ~0.002 $cm^2/(Vs)$ were obtained due to poor surface coverage and film morphology.[30]

Of all functionalized fluorinated ADT derivatives, charge transport in the diF TES-ADT derivative has been studied most extensively, and it is known for its complex behavior of charge carrier dynamics.[21,23,31–35] For example, in one study of *polycrystalline* diF TES-ADT TFTs with gate voltage-dependent room-temperature hole mobilities of up to 0.2 $cm^2/(Vs)$, thermally activated behavior of mobility was observed in the 150-300 K range, followed by an almost temperature-independent behavior at <150 K.[32] The activation energies were 20-100 meV (depending on the gate voltage) in the 215 K-300 K range and somewhat lower in the 150-215 K range. In another study of *polycrystalline* TFTs with a room-temperature mobility of 2.5 $cm^2/(Vs)$, three temperature-dependent regimes were observed: "bandlike" at 200-300 K, with mobility increasing by about 25% as the temperature decreased from 300 K to 200 K, and thermally activated with activation energies (E_a) of 37 meV and 15 meV in the temperature ranges of 150-200 K and 100-150 K, respectively.[34] This study found that the activation energy did not correlate with the charge localization (assessed using charge modulation spectroscopy), and even at low temperatures charge carriers remained mobile within the grains. The authors concluded that the activation energy is related to the grain boundary potential.

On the other hand, in diF TES-ADT *single crystal* FETs with room-temperature mobilities in the 0.8-1.5 $cm^2/(Vs)$ range, thermally activated behavior was observed in the entire range of 220-320 K, with changes in the activation energy occurring at ~260 K and ~300 K such that E_a was 50-105 meV in the 260-300 K range and 18-45 meV at temperatures higher than 300 K and lower than 260 K, depending on the device.[21] This behavior was attributed to a solid-solid phase transition at 294 K, which causes the two crystalline polymorphs to co-exist in the 260-300 K temperature range, while the high-temperature polymorph strongly dominates at temperatures above 300 K and the low-temperature one at temperatures below 260 K.[21]

In this paper, we present a study of photoinduced charge carrier dynamics in diF TES-ADT and diF TSBS-ADT crystals chosen due to their similar molecular properties,[29] but drastically different packing motifs, with an additional feature of a well-documented temperature-dependent polymorph-polymorph transformation in the TES derivative. We relate features in the photoinduced charge carrier transport with crystal structure and disorder.

II. Experimental details

II.1 Materials, sample preparation and structure characterization

The diF TES-ADT single crystal has a triclinic structure with one molecule per unit cell (Z = 1) and unit cell parameters *a* = 7.21 Å (7.12 Å), *b* = 7.32 Å (7.23 Å), *c* = 16.35 Å (16.63 Å), α = 87.72° (97.52°), β = 89.99° (91.36°), γ = 71.94° (107.49°) at temperatures above (below) 294 K, with a solid-solid phase transition occurring at 294 K (Figs. 2 and S1). [4,11,12,18] The diF TSBS-ADT single crystal has a triclinic structure with Z = 4 and unit cell parameters *a* = 15.07 Å, *b* = 16.45 Å, *c* = 18.25 Å, α = 90°, β = 103.06°, γ = 90°. Structures of possible polymorphs of this derivative have not been investigated and are currently unknown.

For crystal growth we used pentafluorobenzenethiol (PFBT)-treated glass substrates with interdigitated Cr/Au electrodes separated by a 25 μm gap.[24,29] A 10 μL droplet of a 30 mM chlorobenzene solution of diF TES-ADT was deposited on the substrate which was then placed in the refrigerator at 275 K and kept in a Parafilm-sealed Petri dish to slow down evaporation. Such procedure yielded crystals of >500 μm length (Fig. 1(b)), which were then imaged using polarization microscopy. Three crystals of each derivative, with as few visible domain boundaries as possible, and positioned on the substrate with the long crystal axis as close as possible to the direction perpendicular to electrodes for consistency (Fig. 1(b)), were selected for the study and characterized using the x-ray diffraction (XRD).

In the case of diF TES-ADT, the XRD (Fig. 1(c)) revealed peaks corresponding to (00*l*) (*l* =1,3,4) orientations, indicative of an ordered molecular structure with a vertical intermolecular spacing of 16.3 Å, consistent with that for the high-temperature polymorph. In the case of diF TSBS-ADT, the (0*ll*) (*l*=1, 2, 3) orientation was observed. Schematics of molecular packing of ADT derivatives under study is shown in Figs. 2 and 3, illustrating the vertical stacking on the substrate (Figs. 2(a) and 3(a)) and the planes where the charge transport occurs in our geometry (Figs. 2(b) and 3(b)). In order to probe the relative degree of crystal imperfections, we performed measurements of the rocking curves on both types of crystals. These revealed a considerably narrower peak (characterized by the FWHM of 0.1°) in diF TES-ADT crystals as compared to that in diF TSBS-ADT crystals (for which a typical FWHM was about 0.8°, Fig. 1(c)), which we attribute to a larger number of defects and broader distribution of domain orientations in diF TSBS-ADT crystals.

Differences in molecular packing of the TES and TSBS derivatives strongly manifest into their optical absorption properties (Fig. 4), resulting in differences in the spectral shape and peak position. For example, the lowest-energy absorption occurred at ~550 nm and ~540 nm in diF TES-ADT and diF TSBS-ADT crystals, respectively, which resulted in differences in crystal appearances (red for the diF TES-ADT and orange for the diF TSBS-ADT crystals). Detailed analysis of molecular packing-dependent optical properties of diF R-ADT crystals will be reported elsewhere. Under unpolarized light excitation, the optical density at the absorption maximum was below 0.4 in all crystals studied.

II.3 Measurements of photocurrent

All measurements of charge carrier dynamics were performed on samples mounted in an optical cryostat (Janis STC-500) and excited from the substrate side. For transient photocurrent measurements, the samples were excited with a circularly polarized beam from a frequency-doubled Q-switched Nd:YAG laser (55 kHz, 470 ps, 532 nm, Altechna STA-01-SH-4-MOPA). Voltage in the range between 10 V and 125 V was applied, and the time-resolved photocurrent was measured using a 50 GHz digital sampling oscilloscope, which enables sub-100 ps time resolution, as described in our previous publications.[24,35,36] The time resolution was limited by the laser pulse width and jitter, so that the rise time (defined here as the 10%-90% time) was about 0.3-0.4 ns in all samples. The incident pulse fluence was varied using a Thorlabs neutral density filter wheel in the 0.47-3.3 μJ/cm^2 range for diF TES-ADT. From the number density of absorbed photons calculated using the pulse fluence and optical absorption at the excitation wavelength, and assuming that the photogeneration efficiency is 5%,[37] this range corresponds to the photoexcited carrier density of (0.3-2.2) x 10^{11} cm^{-2} that should be sufficiently low to minimize high-order effects.[38] The fluence range for diF TSBS-ADT was 0.47-1.3 μJ/cm^2; higher pulse fluences could not be used for this

derivative due to a lower damage threshold as compared to diF TES-ADT. For measurements of photocurrent under continuous wave (cw) excitation, the samples were excited with a circularly polarized beam from a cw 532 nm laser (Coherent Verdi-5) at 2 mW/cm^2, and the current as a function of applied voltage was measured using a Keithley 237 source-measure unit. Current without any photoexcitation was also measured (dark current), and the photocurrent was calculated as the difference between the two.

All experiments were carried out in the temperature range between 80 K and 300 K. Linear photocurrent density (j_{ph}) was calculated using $j_{ph} = I_{ph}/d$, where I_{ph} is the photocurrent and d is the total length of the current-collecting part of the electrode (covered by the crystal), which was determined individually for each sample using optical microscopy images. The average applied electric field F was calculated as $F = V/L$ where V is the applied voltage and L is the gap between the electrodes of 25 μm.

III. Results

Transient photocurrent density obtained with uniform pulsed illumination of diF TES-ADT and diF TSBS-ADT crystals under the same experimental conditions (in particular, pulse fluence of 1.2 μJ/cm^2, applied electric field of 40 kV/cm, and temperature of 300 K) are shown in Fig. 5. The peak photocurrent density observed in diF TES-ADT crystals was more than an order of magnitude higher than that in polycrystalline diF TES-ADT films[24] due to higher charge carrier mobility and lower carrier loss in traps in the first several hundreds of picoseconds in crystals as compared to films. Importantly, about an order of magnitude higher peak photocurrent density was obtained in the TES derivative as compared to TSBS, which we attribute primarily to differences in average intrinsic charge carrier mobilities in the corresponding charge transport planes (Figs. 2(b) and 3(b)) assessed in our experimental geometry.

Figure 6 shows dependence of the photocurrent in a diF TES-ADT crystal on the pulse fluence (I) at 300 K. The peak photocurrent (I_{ph}) exhibited a power-law behavior $I_{ph} \sim I^a$ with a = 0.78 ± 0.01 (inset of Fig. 6), indicative of a contribution of shallow traps to charge transport already at sub-0.4 ns time-scales after photoexcitation. This is consistent with observations of charge trapping occurring on the sub-100 ps time scales in other molecular crystals such as pentacene or tetracene.[39,40] At low temperatures, similar pulse fluence dependence was observed (e.g. a = 0.80 ± 0.05 at 80 K) which suggests that a similar charge transport mechanism is operational in the entire temperature range of 80-300 K.

Temperature dependence of the photocurrent obtained from diF TES-ADT crystals supports the hypothesis of contributions of charge traps into transport. This can be appreciated from Fig. 7(a) that shows thermally activated behavior of the peak photocurrent (which we denote to occur at t = 0 for all discussions that follow). The activation energy (E_a) (obtained from fits of the peak transient photocurrent with an Arrhenius-type function so that $I_{ph} \propto \exp(-E_a/k_BT)$, where k_B is the Boltzmann constant and T is the temperature) sharply decreased at temperatures below ~230 K (inset of Fig. 7(a)). For example, at the applied electric field of 40 kV/cm, the activation energy E_a in the 230-300 K range at t = 0 was 17 ± 4 meV, in contrast to only 2.2 ± 0.4 meV at 80-230 K.

The activation energy E_a relatively weakly depended on the pulse fluence (and thus, photoexcited charge carrier density); for example, an increase in the pulse fluence by a factor of ~7 resulted in the decrease in

E_a from 19 meV to 14 meV, at 40 kV/cm in the 230-300 K temperature range. However, a considerably stronger dependence of the activation energy on the applied electric field was observed (Fig. 7(c)) in this temperature range, with the E_a decreasing as the applied electric field (*F*) increased. This dependence could be well described in the framework of electrostatic energy barrier lowering due to the Poole-Frenkel effect, in the form of $E_a = E_a^0 - \beta\sqrt{F}$ (where E_a^0 is the zero field activation energy and β is a parameter). Fits of the diF TES-ADT data by this equation in the 230-300 K temperature range yielded the zero field activation energy E_a^0 of 48 ± 2 meV and $\beta = (1.6 \pm 0.1) \times 10^{-4}$ eV $(cm/V)^{1/2}$. The obtained value of E_a^0 will be discussed in the next section. The obtained value of β is lower than the Poole-Frenkel factor ($\beta_{PF} = (7.59 \times 10^{-4})/\sqrt{\varepsilon}$ eV$(cm/V)^{1/2}$, where ε is the dielectric constant), as β_{PF} of ~4×10^{-4} eV$(cm/V)^{1/2}$ would be expected for a typical value of $\varepsilon = 3.5$. Instead, it is consistent with the modified Poole-Frenkel factor previously introduced to describe electric field dependence of the current in which the field dependence of free carrier density is coupled with that of carrier mobility in crystalline materials (for example, $\beta = (2 \pm 1) \times 10^{-4}$ eV $(cm/V)^{1/2}$ was obtained in crystalline perylene diimide).[41]

In diF TES-ADT crystals, the decay dynamics was weakly temperature dependent (Fig. 8(a)), with the most change in the decay dynamics occurring in the 230-300 K temperature range, mimicking the behavior of the peak photocurrent (inset of Fig. 7(a)). For example, at 40 kV/cm the activation energy E_a obtained from Arrhenius fits to the photocurrent density at t = 0 ns, 1 ns, and 8 ns was E_a = (17 ± 4) meV, (24 ± 7) meV, and (30 ± 3) meV, respectively, in the 230-300 K range, while it was in the range of 1-2 meV at lower temperatures for any time *t* within our experimental range (*t* < 10 ns). Relatively small temperature-dependent change in the nanosecond time-scale dynamics suggests that most carriers that are able to contribute to charge transport at room temperature at these time scales are also mobile at low temperatures, in agreement with observations of Ref. [34].

The diF TSBS-ADT crystals showed several qualitative similarities in the transient photocurrent to that in diF TES-ADT crystals. For example, the pulse fluence dependence of the peak photocurrent ($I_{ph} \sim I^a$) was also slightly sublinear, with a = 0.90 ± 0.06. Also, the temperature dependence of the photocurrent exhibited a larger activation energy E_a in the 200-300 K temperature range, increasing with time *t*, followed by an almost temperature-independent behavior at lower temperatures (Fig. 7(b)). For example, at 40 kV/cm the activation energy E_a was <2 meV at *t* = 0, then 6 ± 1 meV at t = 0.35 ns, and 12 ± 4 meV at 1 ns at 200-300K and <1 meV at lower temperatures for any *t* (inset of Fig. 7(b)). The fits to the electric field dependence of the activation energy (Fig. 7(c)) observed at *t* = 0.35 ns in the 200-300 K temperature range using the Poole-Frenkel expression discussed above yielded $E_a^0 =$ (42 ± 10) meV and $\beta = (1.7 \pm 0.5) \times 10^{-4}$ eV $(cm/V)^{1/2}$, both values comparable to those obtained for diF TES-ADT crystals at t <0.5 ns in the 230-300 K range. Interestingly, in contrast to diF TES-ADT, the diF TSBS-ADT crystals exhibited a more uniform temperature-dependent behavior of the peak photocurrent, with E_a < 2 meV at 40 kV/cm (inset of Fig. 7(b)) in the entire temperature range of 80-300 K, and most temperature dependent change in the photocurrent occurred at longer time scales (t > 0.1 ns). The latter manifested through a considerably more pronounced temperature dependence of the decay dynamics in diF TSBS-ADT crystals (Fig. 8(b)) as compared to that in diF TES-ADT crystals (Fig. 8(a)).

Linear photocurrent densities (j_{cw}) obtained using 532 nm cw excitation of the crystals at 2 mW/cm^2, at various applied electric fields and temperatures, are shown in Fig. 9. In both diF TES-ADT and diF TSBS-ADT crystals, dark current densities were a factor of ~2 (>10) lower than the photocurrent densities at 300

K (100 K). Thermally activated behavior of the cw photocurrent was observed in both diF TES-ADT and diF TSBS-ADT crystals throughout the entire temperature range of 80-300 K, with an activation energy (E_a) of (16 ± 4) meV that did not appreciably change with the applied electric field. At 300 K, the cw photocurrent densities obtained in diF TES-ADT and diF TSBS-ADT crystals differed by a factor of ~250, which is considerably higher than a difference of a factor of ~12 obtained in the same samples under the pulsed excitation at t = 0 in Fig. 5.

IV. Discussion

Time-resolved photoconductivity has served as an important tool for understanding charge carrier dynamics in organic semiconductors including molecular crystals as it enables insight into initial charge dynamics, immediately after excitation into delocalized states and prior to considerable trapping.[35,37,40,42,43] From the peak photocurrent, one obtains the product of the sum of hole and electron mobilities (dominated in ADT derivatives under study by the hole mobility, μ) and the photogeneration efficiency (η) as follows: $\mu\eta = j_{ph}/(N_{ph}\, e\, F)$, where j_{ph} is the linear photocurrent density, N_{ph} is the absorbed photon density, e is the electric charge, and F is the applied electric field.[37] Here η includes any carrier losses that occurred within the first several hundreds of picoseconds not resolved in our experiments. From peak photocurrents measured at 300 K and 40 kV/cm, the $\mu\eta$ values of 0.1-0.14 $cm^2/(Vs)$ and 0.006-0.007 $cm^2/(Vs)$ were obtained for the diF TES-ADT and diF TSBS-ADT crystals, respectively. The $\mu\eta$ values in diF TES-ADT crystals are more than an order of magnitude higher than those in polycrystalline diF TES-ADT films[24] due to higher mobility μ and lower initial charge carrier loss (which is incorporated in η) in crystals. At 80 K, the $\mu\eta$ values were about a factor of 2 lower than those at 300 K, yielding 0.045-0.092 $cm^2/(Vs)$ and 0.003-0.004 $cm^2/(Vs)$) in diF TES-ADT and diF TSBS-ADT crystals, respectively.

Although in our experiments μ and η cannot be separated, in the following estimates we use the temperature-independent value of η = 0.05 for both derivatives. This choice was motivated by the following considerations. Values of 0.05 and 0.04 were obtained in similar transient photoconductivity experiments on tetracene single crystals[37] and in transient photocurrent measurements combined with numerical simulations (which enable separate determination of the initial ultrafast charge separation efficiency and the mobility) in diF TES-ADT films,[35] respectively. Additionally, our previous work with diF R-ADT and R-Pn derivatives[22,44] revealed that η in these crystalline materials is considerably less sensitive to the molecular packing as compared to charge carrier mobility. For example, in crystals with packing motifs featuring more than an order of magnitude anisotropy of mobility, the anisotropy of the photogeneration efficiency was within a factor of 2, regardless of the excitation wavelength.[44] Therefore, similar initial charge separation efficiencies in both ADT derivatives under study would be expected. Finally, the initial (sub-0.4 ns) carrier trapping should not considerably contribute to the value of η as carriers in diF TES-ADT trapped in shallow traps are mobile whereas carriers in diF TSBS-ADT are trapped at longer time scales and thus are also mobile initially, as discussed below. This leads to a low initial carrier loss in both derivatives. With these considerations, the temperature dependence of the peak photocurrent is solely due to that of the mobility, which is consistent with the data being well-described by the Poole-Frenkel formalism as discussed above and with similar previous observations in diF TES-ADT films.[23] From the $\mu\eta$ values extracted from the peak photocurrent the hole mobility is then estimated to be 2.0-2.8 $cm^2/(Vs)$ (0.9-1.8 $cm^2/(Vs)$) in diF TES-ADT crystals and 0.13-0.14 $cm^2/(Vs)$ (0.06-0.08 $cm^2/(Vs)$) in diF TSBS-ADT crystals at 300 K (80 K). The 300 K mobility values obtained for diF TES-ADT compare well

with diF TES-ADT single crystal FET mobilities which were in the 1-6 $cm^2/(Vs)$ range, depending on the crystal quality.[17] While single crystals of diF TSBS-ADT have not been previously studied, our values obtained for this derivative are considerably higher than those of ≤0.002 $cm^2/(Vs)$ observed in poor-morphology polycrystalline diF TSBS-ADT TFTs, as expected.[30]

Mechanisms of charge transport in organic crystals have been under intense debate,[1] with no consensus yet reached on the origin of "bandlike" temperature dependence of mobility (with the mobility decreasing with temperature) often observed even along a "slow" axis (e.g. along the *c*-axis of naphthalene or rubrene, with room-temperature mobilities of 0.2-0.3 $cm^2/(Vs)$ [1,45]). Additionally, several charge transport pathways could often be enabled, with charge transport proceeding both in the extended states and via localized states, which could manifest differently depending on the experimental tool and conditions. [7,46,47] For example, in polycrystalline films, a change from thermally activated mobility at higher temperatures to the temperature-independent behavior at lower temperatures has been observed in various materials. [32,48,49] Such behavior was consistent with a change in the dominant transport mechanism from transport in the extended states (described by the mobility edge model that involves thermal activation of carriers from shallow traps to the band) at higher temperatures to a non-activated carrier motion through the band tail states at low temperatures. In charge-transfer crystals, [50] a similar temperature dependence of mobility was observed, and the activation energy change was related to the glass transition, so that temperature-independent mobility at low temperatures was attributed to a frozen-in orientational disorder. In polycrystalline octithiophene FETs, a change in activation energy was taken as a feature of the grain boundary-limited transport so that thermal activation over the grain boundaries at high temperatures is replaced by non-activated tunneling at low temperatures. [49]

In our case, "bandlike" behavior was not observed in either of the crystals studied, which suggests that even at the earliest time of our detection, shallow traps (that are filled within the first several hundreds of picoseconds after photoexcitation, not resolved in our measurements) contribute to the observed photocurrent. Nevertheless, thermal activation energies observed at <1 ns after photoexcitation were relatively low (Fig. 7). Because the mobility values extracted from the data at 300 K and 80 K were similar (within a factor of 1.5-2) in both diF TES-ADT and diF TSBS-ADT crystals, it appears unlikely that two distinctly different transport mechanisms, such as transport in the extended states and via the localized band tail states, would be involved in transport at high and at low temperatures, respectively. Additionally, given overall similarities in the temperature and intensity dependence of the sub-1 ns photocurrents in both types of crystals, we hypothesize that the charge transport mechanism is the same in these crystals, even though the observed mobilities are considerably different. We consider that carrier (hole) motion immediately after photoexcitation occurs in the extended states of the valence band at all temperatures in both diF TES-ADT and diF TSBS-ADT crystals. The shallow traps serve as a source of carriers that are thermally excited, with assistance from the applied electric field via Poole-Frenkel mechanism, to the band edge. A higher mobility in the (001) plane of the diF TES-ADT crystal as compared to that in the (011) plane of the diF TSBS-ADT crystal would be expected based on the molecular packing (Figs. 2(b) and 3(b)) featuring stronger π–π overlap in the "brickwork" packing of the TES derivative over that in the "sandwich-herringbone" packing of the TSBS derivative. We note, however, that because of the domain distribution (manifested in the width of the rocking curve of Fig. 1(c)), the obtained mobility estimates represent values averaged over the domains. This is especially important in the case of the TSBS

derivative with 1D transport, for which the obtained mobility estimates serve as lower bounds for the mobility along the most efficient charge transport direction.

Next, we address the nature of traps in our crystals. In diF TES-ADT crystals, a sharp change in the activation energy for charge carrier mobility has been previously observed in the FET data and attributed to a reversible solid-solid phase transition.[21] In particular, at temperatures above 295 K (below 240 K), only the high-temperature (low-temperature) polymorph was shown to exist, whereas in the temperature region between ~240 K and ~295 K, two polymorphs co-existed. The charge transport in this intermediate temperature range was observed to be thermally activated with a considerably higher activation energy than that at either lower or higher temperatures.[21] Our data are consistent with this description, and the shallow traps that contributed to an activated photocurrent with the zero-field activation energy of 48 meV (Fig. 7) at 230-300 K could be associated with defects caused by the co-existence of the two polymorphs. Then, the obtained hole mobilities at 300 K (2.8 $cm^2/(Vs)$) and 80 K (1.8 $cm^2/(Vs)$) would represent mobilities in the high-temperature and low-temperature polymorph, respectively, and considerably weaker temperature dependence of mobility would be expected in the pure phases (>300 K and <230 K), just as seen in the low-temperature data. A slightly lower mobility in the low-temperature diF TES-ADT polymorph (Fig. S1) as compared to the high-temperature polymorph is consistent with findings of Ref. [21] in single-crystal diF TES-ADT FETs. Since the structure change in the *a-b* plane of the crystal is relatively subtle (Figs. 2 and S1) and reversible, formation of large density of deep traps as a result of the polymorph-polymorph phase transition in this case would not be expected.

In the diF TSBS-ADT crystals, the photocurrent at t = 0 exhibited a uniform temperature dependence across the entire temperature range studied, with a very small activation energy (<2 meV in Fig. 7(b)). However, at t > 0.1 ns two distinct behaviors, similar to those in diF TES-ADT, were observed: thermally activated transport with an applied field-dependent activation energy at temperatures between 200 K and 300 K, followed by the temperature independent behavior at lower temperatures. Similarity of the behavior and of activation energies between these two ADT derivatives may suggest the possibility of a similar polymorph-polymorph phase transition occurring in the diF TSBS-ADT as well. In this case, charge carrier mobilities of 0.14 $cm^2/(Vs)$ at 300 K and 0.08 $cm^2/(Vs)$ at 80 K would represent those in the high-temperature and low-temperature polymorphs, respectively. However, temperature-dependent XRD analysis of the diF TSBS-ADT derivative would be needed to confirm the polymorph-polymorph transition or other structural transformation occurring in this temperature range. Regardless of the exact nature of the transformation, it is responsible for creating defects serving as shallow traps and leading to a factor of ~1.8 lower mobility at 80 K as compared to that at 300 K in diF TSBS-ADT crystals.

One distinct feature observed in diF TSBS-ADT crystals as compared to diF TES-ADT is the dynamics of carrier trapping and their subsequent excitation to transport states as manifested in the temperature-dependent photocurrent decays. In diF TES-ADT, already at t = 0 many charge carriers were trapped by shallow traps, but could participate in charge transport by excitation to the extended states; most of the carriers that were available for nanosecond time-scale charge transport at 300 K were also able to participate in transport at low temperatures (Fig. 8(a)). In contrast, in diF TSBS-ADT crystals, shallow trap filling occurred throughout the nanosecond time scales, with a pronounced mobile carrier loss occurring at low temperatures (Fig. 8(b)). Such differences in carrier trapping and detrapping dynamics could be

related to the lower charge carrier mobility in diF TSBS-ADT as compared to diF TES-ADT and dimensionality of charge transport (1D in the TSBS and 2D in the TES derivatives), respectively.[51]

Progressive carrier localization and ultimate trapping in deep traps which reduce the density of mobile charge carriers at all temperatures in diF TSBS-ADT are also behind the increasing difference in photocurrent densities observed in diF TSBS-ADT and diF TES-ADT crystals at longer time scales: from a factor of ~12 at t = 0 under pulsed excitation (Fig. 5) to a factor of ~250 in the steady-state under cw excitation (Fig. 9) at 300 K, in the same crystals. While the difference at t = 0 is mostly due to differences in intrinsic mobilities between the two derivatives determined by the molecular packing, the additional order of magnitude difference in the equilibrium is due to the carrier loss in deep traps. The origin of such deep traps is most likely related to domain boundaries which would be expected to be more pronounced in diF TSBS-ADT as compared to diF TES-ADT based on the rocking curves revealed by the XRD (inset of Fig. 1(c)).

Interestingly, the photoinduced charge transport under steady-state excitation conditions was thermally activated with an electric field-independent, low (16 ± 4 meV) activation energy throughout the entire temperature range for both derivatives (Fig. 9). Such lack of sensitivity of the cw photocurrent to the temperature dependent structural transformation such as a polymorph-polymorph phase transition suggests that in this regime the transport level moves away from the band edge into the band tail[52] and the charge transport is determined by the properties of the states in the band tail that are not profoundly influenced by the structural transformations occurring in the 230-300 K (200-300 K) temperature range in the TES (TSBS) derivative that are responsible for the formation of shallow traps probed by the transient photocurrent measurements. Similarity of activation energies in the photocurrent obtained in both derivatives suggests similarity of the states that contribute to charge transport at the equilibrium; however, significant loss of carriers into deep traps in diF TSBS-ADT that are not able to contribute mobile carriers even at room temperature are responsible for considerably lower cw photocurrents in diF TSBS-ADT as compared to diF TES-ADT.

Conclusions

Analysis of photoinduced charge carrier dynamics in single crystals of two ADT derivatives featuring 2D “brickwork” and 1D “sandwich-herringbone” packing revealed similarities in the shallow charge trap characteristics and differences in intrinsic charge carrier mobilities, charge trapping and detrapping dynamics, and in the deep trap characteristics. Charge carrier mobilities of 2.0-2.8 $cm^2/(Vs)$ and 0.13-0.14 $cm^2/(Vs)$ were obtained at 300 K in diF TES-ADT and diF TSBS-ADT crystals, respectively. The differences in mobility were attributed to those in the molecular packing, with the TES derivative characterized by a more efficient 2D charge transport as compared to 1D transport in the TSBS derivative. These differences led to a more pronounced nanosecond time-scale carrier localization at low temperatures in the TSBS derivative as compared to TES. Temperature-induced structural changes occurring in the 230-300 K (200-300 K) temperature range in diF TES-ADT (diF TSBS-ADT) crystals introduced shallow traps that could be described via exponential distribution with a characteristic energy of ~40-50 meV in both types of crystals. At temperatures below 200 K, an almost temperature-independent charge transport was observed, with mobilities of 0.9-1.8 $cm^2/(Vs)$ (0.06-0.08 $cm^2/(Vs)$) for diF TES-ADT (diF TSBS-ADT) crystals at 80 K. Comparison of the photocurrent densities revealed the difference by a factor ~12 at t = 0 (with diF TES-

ADT exhibiting a higher photocurrent density than diF TSBS-ADT) that increased to a factor of ~250 in the equilibrium. This observation is attributed to the presence of deep traps in the TSBS derivative, most likely related to domain boundaries more prominent in diF TSBS crystals as compared to diF TES-ADT.

Acknowledgments

We thank Prof. O. Jurchescu for providing a calibration diF TES-ADT single crystal sample and Prof. M. Graham for help with imaging the crystals. Financial support from the National Science Foundations (DMR-1207309 and DMR-1808258) is gratefully acknowledged.

Declarations of interest: none

Supporting information contains a figure showing molecular packing in the low-temperature polymorph of diF TES-ADT.

References

1. Ostroverkhova, O. Organic optoelectronic materials : mechanisms and applications. *Chem. Rev.* **116,** 13279–13412 (2016).
2. Troisi, A. & Orlandi, G. Charge-transport regime of crystalline organic semiconductors: Diffusion limited by thermal off-diagonal electronic disorder. *Phys. Rev. Lett.* **96,** 86601 (2006).
3. Jiang, Y. *et al.* Nuclear quantum tunnelling and carrier delocalization effects to bridge the gap between hopping and bandlike behaviors in organic semiconductors. *Nanoscale Horiz.* **1,** 53–59 (2016).
4. Li, Y., Yi, Y., Coropceanu, V. & Brédas, J. L. Symmetry effects on nonlocal electron-phonon coupling in organic semiconductors. *Phys. Rev. B* **85,** 245201 (2012).
5. Ciuchi, S. *et al.* Molecular fingerprints in the electronic properties of crystalline organic semiconductors: From experiment to theory. *Phys. Rev. Lett.* **108,** 256401 (2012).
6. Fratini, S., Mayou, D. & Ciuchi, S. The Transient Localization Scenario for Charge Transport in Crystalline Organic Materials. *Adv. Funct. Mater.* **26,** 2292–2315 (2016).
7. Yi, H. T., Garstein, Y. N. & Podzorov, V. Charge carrier coherence and Hall effect in organic semiconductors. *Sci. Rep.* **6,** 23650 (2016).
8. Yavuz, I., Martin, B. N., Park, J. & Houk, K. N. Theoretical study of the molecular ordering, paracrystallinity, and charge mobilities of oligomers in different crystalline phases. *J. Am. Chem. Soc.* **137,** 2856–2866 (2015).
9. Sokolov, A. N. *et al.* From computational discovery to experimental characterization of a high hole mobility organic crystal. *Nat. Commun.* **2,** 437 (2011).
10. Illig, S. *et al.* Reducing dynamic disorder in small-molecule organic semiconductors by suppressing large-amplitude thermal motions. *Nat. Commun.* **7,** 10736 (2016).

11. Krupskaya, Y., Gibertini, M., Marzari, N. & Morpurgo, A. F. Band-Like Electron Transport with Record-High Mobility in the TCNQ Family. *Adv. Mater.* **27,** 2453–2458 (2015).

12. Chernyshov, I. Y., Vener, M. V, Feldman, E. V, Paraschuk, D. Y. & Sosorev, A. Y. Inhibiting Low-Frequency Vibrations Explains Exceptionally High Electron Mobility in 2,5-Di fluoro-7,7,8,8-tetracyanoquinodimethane (F2-TCNQ) Single Crystals. *J. Phys. Chem. Lett.* **8,** 2875–2880 (2017).

13. Stevens, L. A., Goetz, K. P., Fonari, A., Shu, Y. & Williamson, R. M. Temperature-Mediated Polymorphism in Molecular Crystals : The Impact on Crystal Packing and Charge Transport. *Chem. Mater.* **27,** 112–118 (2015).

14. Burnett, E. K. *et al.* Bistetracene Thin Film Polymorphic Control to Unravel the Effect of Molecular Packing on Charge Transport. *Adv. Mater. Interfaces* **5,** 1701607 (2018).

15. Hsieh, C. *et al.* Polymorphic Behavior of Perylene and Its In fl uences on OFET Performances. *J. Phys. Chem. C* **122,** 16242–16248 (2018).

16. Kline, R. J. *et al.* Controlling the microstructure of solution-processable small molecules in thin-film transistors through substrate chemistry. *Chem. Mater.* **23,** 1194–1203 (2011).

17. Jurchescu, O. D. *et al.* Organic single-crystal field-effect transistors of a soluble anthradithiophene. *Chem. Mater.* **20,** 6733–6737 (2008).

18. Hallani, R. K. *et al.* Structural and Electronic Properties of Crystalline, Isomerically Pure Anthradithiophene Derivatives. *Adv. Funct. Mater.* **26,** 2341–2348 (2016).

19. Li, R. *et al.* Direct structural mapping of organic field-effect transistors reveals bottlenecks to carrier transport. *Adv. Mater.* **24,** 5553–5558 (2012).

20. Diemer, P. J. *et al.* Vibration-assisted crystallization improves organic/dielectric interface in organic thin-film transistors. *Adv. Mater.* **25,** 6956–6962 (2013).

21. Jurchescu, O. *et al.* Effects of polymorphism on charge transport in organic semiconductors. *Phys. Rev. B* **80,** 85201 (2009).

22. Platt, A. D., Day, J., Subramanian, S., Anthony, J. E. & Ostroverkhova, O. Optical, fluorescent, and (photo)conductive properties of high-performance functionalized pentacene and anthradithiophene derivatives. *J. Phys. Chem. C* **113,** 14006–14014 (2009).

23. Platt, A., Kendrick, M., Loth, M., Anthony, J. & Ostroverkhova, O. Temperature dependence of exciton and charge carrier dynamics in organic thin films. *Phys. Rev. B* **84,** 235209 (2011).

24. Paudel, K. *et al.* Enhanced charge photogeneration promoted by crystallinity in small-molecule donor-acceptor bulk heterojunctions. *Appl. Phys. Lett.* **105,** 43301 (2014).

25. Guo, W. *et al.* Solution-processed low-voltage organic phototransistors based on an anthradithiophene molecular solid. *Org. Electron.* **15,** 3061–3069 (2014).

26. Lim, B. T., Cho, J., Cheon, K. H., Shin, K. & Chung, D. S. Photoconductive behaviors of difluorinated 5,11-bis(triethylsilylethynyl) anthradithiophene. *Org. Electron.* **18,** 113–117 (2015).

27. Kim, J., Cho, S., Kim, Y.-H. & Park, S. K. Highly-sensitive solution-processed 2,8-difluoro-5,11-bis(triethylsilylethynyl) anthradithiophene (diF-TESADT) phototransistors for optical sensing applications. *Org. Electron.* **15,** 2099–2106 (2014).

28. Niazi, M. R. *et al.* Solution-printed organic semiconductor blends exhibiting transport properties on par with single crystals. *Nat. Commun.* **6,** 8598 (2015).

29. Paudel, K. *et al.* Small-molecule bulk heterojunctions: Distinguishing between effects of energy offsets and molecular packing on optoelectronic properties. *J. Phys. Chem. C* **117,** 24752–24760 (2013).

30. Goetz, K. P. *et al.* Effect of acene length on electronic properties in 5-, 6-, and 7-ringed heteroacenes. *Adv. Mater.* **23,** 3698–3703 (2011).

31. Hunter, S. & Anthopoulos, T. D. Observation of unusual, highly conductive grain boundaries in high-mobility phase separated organic semiconducting blend films probed by lateral-transport conductive-AFM. *Adv. Mater.* **25,** 4320–4326 (2013).

32. Hunter, S., Chen, J. & Anthopoulos, T. D. Microstructural control of charge transport in organic blend thin-film transistors. *Adv. Funct. Mater.* **24,** 5969–5976 (2014).

33. Smith, J. *et al.* Solution-processed small molecule-polymer blend organic thin-film transistors with hole mobility greater than 5 cm 2/Vs. *Adv. Mater.* **24,** 2441–2446 (2012).

34. Meneau, A. Y. B. *et al.* Temperature Dependence of Charge Localization in High-Mobility , Solution-Crystallized Small Molecule Semiconductors Studied by Charge Modulation Spectroscopy. *Adv. Funct. Mater.* **26,** 2326–2333 (2016).

35. Johnson, B., Kendrick, M. J. & Ostroverkhova, O. Charge carrier dynamics in organic semiconductors and their donor-acceptor composites: Numerical modeling of time-resolved photocurrent. *J. Appl. Phys.* **114,** 94508 (2013).

36. Day, J. *et al.* Photoconductivity in organic thin films: From picoseconds to seconds after excitation. *J. Appl. Phys.* **103,** 123715 (2008).

37. Moses, D., Soci, C., Chi, X. & Ramirez, A. P. Mechanism of carrier photogeneration and carrier transport in molecular crystal tetracene. *Phys. Rev. Lett.* **97,** 67401 (2006).

38. Reid, O. G., Pensack, R. D., Song, Y., Scholes, G. D. & Rumbles, G. Charge photogeneration in neat conjugated polymers. *Chem. Mater.* **26,** 561–575 (2014).

39. Ostroverkhova, O. *et al.* Optical and transient photoconductive properties of pentacene and functionalized pentacene thin films: Dependence on film morphology. *J. Appl. Phys.* **98,** 33701 (2005).

40. Ostroverkhova, O. *et al.* Ultrafast carrier dynamics in pentacene, functionalized pentacene, tetracene, and rubrene single crystals. *Appl. Phys. Lett.* **88,** 162101 (2006).

41. Chen, S., Stradins, P. & Gregg, B. A. Doping Highly Ordered Organic Semiconductors: Experimental Results and Fits to a Self-Consistent Model of Excitonic Processes, Doping, and Transport. 13451–13460 (2005).

42. Spencer, S. *et al.* Critical electron transfer rates for exciton dissociation governed by extent of crystallinity in small molecule organic photovoltaics. *J. Phys. Chem. C* **118,** 14848–14852 (2014).

43. Najafov, H., Biaggio, I., Podzorov, V., Calhoun, M. F. & Gershenson, M. E. Primary photoexcitations and the origin of the photocurrent in rubrene single crystals. *Phys. Rev. Lett.* **96,** 56604 (2006).

44. Ostroverkhova, O. *et al*. Anisotropy of transient photoconductivity in functionalized pentacene single crystals. *Appl. Phys. Lett.* **89**, 192113 (2006).

45. Blulle, B., Troisi, A., Hausermann, R. & Batlogg, B. Charge transport perpendicular to the high mobility plane in organic crystals: bandlike temperature dependence maintained despite hundredfold anisotropy. *Phys. Rev. B* **93,** 35205 (2016).

46. Mehraeen, S., Coropceanu, V. & Bredas, J. L. Role of band states and trap states in the electrical properties of organic semiconductors: Hopping versus mobility edge model. *Phys. Rev. B - Condens. Matter Mater. Phys.* **87,** 195209 (2013).

47. Xie, H., Alves, H. & Morpurgo, A. Quantitative analysis of density-dependent transport in tetramethyltetraselenafulvalene single-crystal transistors: intrinsic properties and trapping. *Phys. Rev. B* **80,** 245305 (2009).

48. Street, R. A., Northrup, J. E. & Salleo, A. Transport in polycrystalline polymer thin-film transistors. *Phys. Rev. B* **71,** 165202 (2005).

49. Bourguiga, R. *et al.* Charge transport limited by grain boundaries in polycrystalline octithiophene thin film transistors. *Eur. Phys. J. AP* **19,** 117–122 (2002).

50. Goetz, K. P. *et al.* Freezing-in orientational disorder induces crossover from thermally-activated to temperature-independent transport in organic semiconductors. *Nat. Commun.* **5,** 5642 (2014).

51. Steiner, F. *et al.* Influence of orientation mismatch on charge transport across grain boundaries in tri- isopropylsilylethynyl (TIPS) pentacene thin films. *Phys. Chem. Chem. Phys.* **19,** 10854–10862 (2017).

52. Baranovskii, S. D. Theoretical description of charge transport in disordered organic semiconductors. *Phys. Status Solidi* **251,** 487–525 (2014).

Figure captions

Figure 1. (a) ADT derivatives under study. (b) Images of solution-grown ADT crystals on interdigitated electrodes (vertical lines) spaced by 25 μm. Red line corresponds to a “long crystal axis” and the direction of applied electric field. (c) XRD data on representative diF TES-ADT and diF TSBS-ADT crystals. Inset shows rocking curves.

Figure 2. Molecular packing of the diF TES-ADT derivative. (a) Side view; black line corresponds to the substrate. The substrate coincides with the (001) crystal orientation. (b) Top view of the plane in which the charge transport is measured in our experiments. Side groups are cropped for clarity. Crystal axes are also shown.

Figure 3. Molecular packing of the diF TSBS-ADT derivative. (a) Side view; black line corresponds to the substrate. The substrate coincides with the (011) crystal orientation. (b) Top view of the plane in which

the charge transport is measured in our experiments. Side groups are cropped for clarity. Crystal axes are also shown.

Figure 4. Optical absorption spectra of representative diF TES-ADT and diF TSBS-ADT crystals. Optical absorption from a dilute solution of diF TES-ADT (identical to that of diF TSBS-ADT) in toluene is also shown.

Figure 5. Time-resolved photocurrent density obtained under 532 nm pulsed excitation at the pulse fluence of 1.2 $\mu J/cm^2$ and applied electric field of 40 kV/cm at 300 K.

Figure 6. Time-resolved photocurrent in diF TES-ADT at 300 K at various excitation pulse fluences (2.8 $\mu J/cm^2$, 2.4 $\mu J/cm^2$, 1.9 $\mu J/cm^2$, 1.4 $\mu J/cm^2$, 0.94 $\mu J/cm^2$, and 0.47 $\mu J/cm^2$). Inset shows photocurrent peak dependence on the fluence.

Figure 7. Time-resolved photocurrent in (a) diF TES-ADT and (b) diF TSBS-ADT at various temperatures at 40 kV/cm: 300 K, 280 K, 230 K, 130 K, and 80 K in (a) and 300 K, 200 K, 150 K, and 80 K in (b). Insets show temperature dependence of photocurrent densities at various times after photoexcitation. Arrhenius fits are also included. Fit parameters are discussed in the text. The time t = 0 corresponds to the time at which the peak photocurrent occurs. (c) Activation energies extracted from fits of temperature dependent data at different applied electric fields at t = 0 in diF TES-ADT and t = 0.35 ns in diF TSBS-ADT in the 230-300 K and 200-300 K temperature ranges, respectively. Fits to the Poole-Frenkel equation and the zero field activation energies determined from the fit are also shown.

Figure 8. Normalized photocurrents at various temperatures in (a) diF TES-ADT and (b) diF TSBS-ADT crystals.

Figure 9. Photocurrent densities obtained under 532 nm 2 mW/cm^2 cw excitation as a function of applied electric field at various temperatures in diF TES-ADT and diF TSBS-ADT crystals. Inset shows temperature dependence of photocurrent densities measured at 40 kV/cm in both types of crystals. Arrhenius fits and activation energies are also included.

Figures

Figure 1

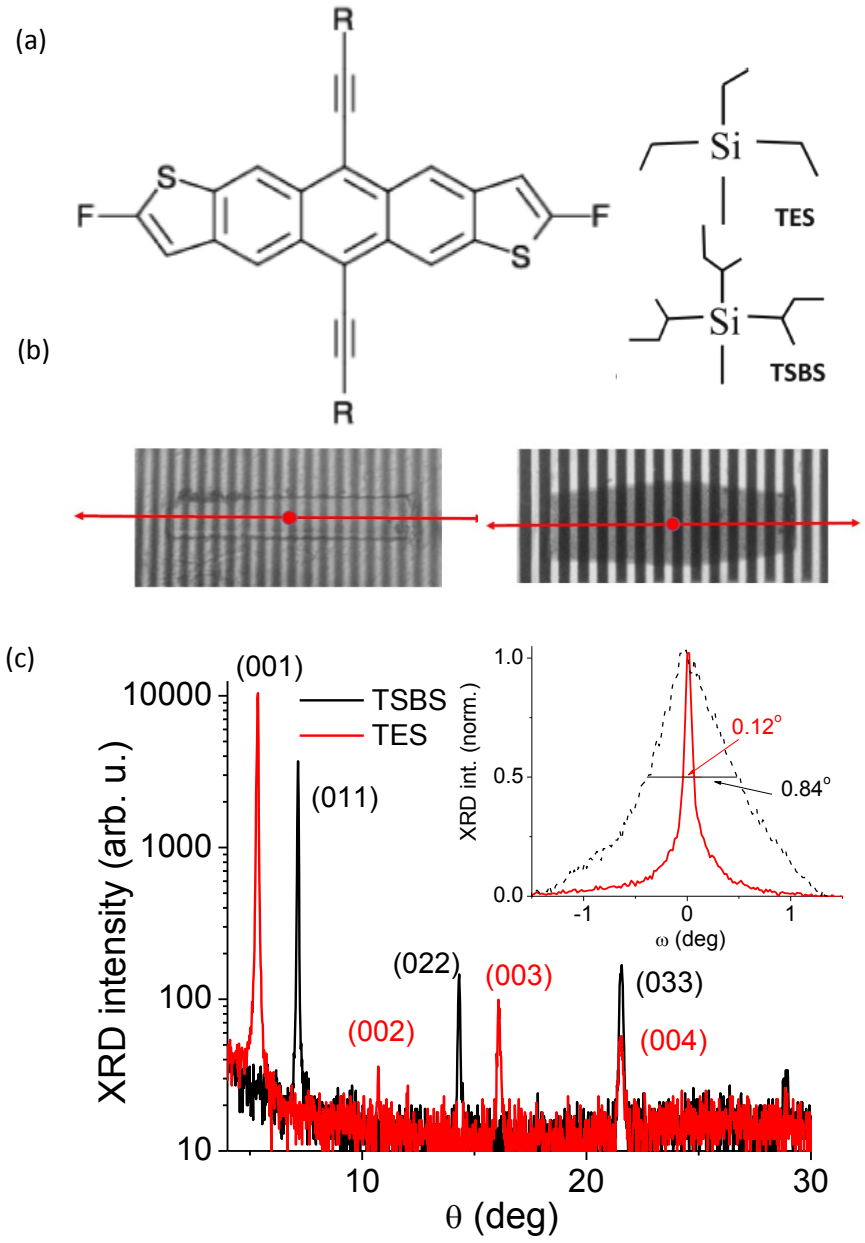

Figure 2

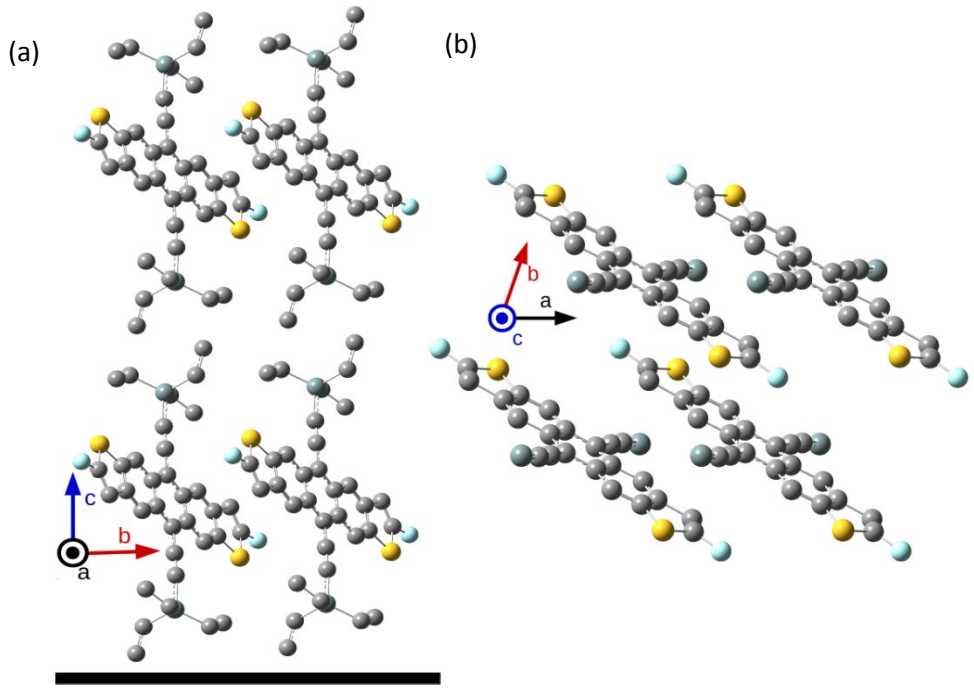

Figure 3

(a)

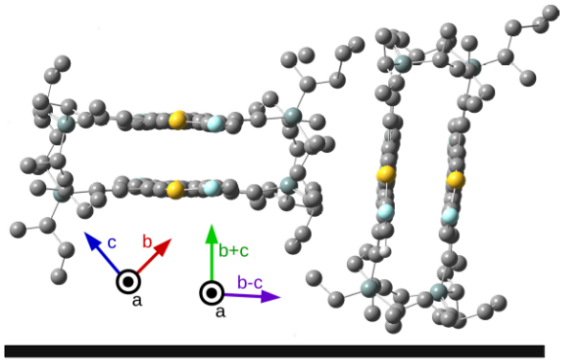

(b)

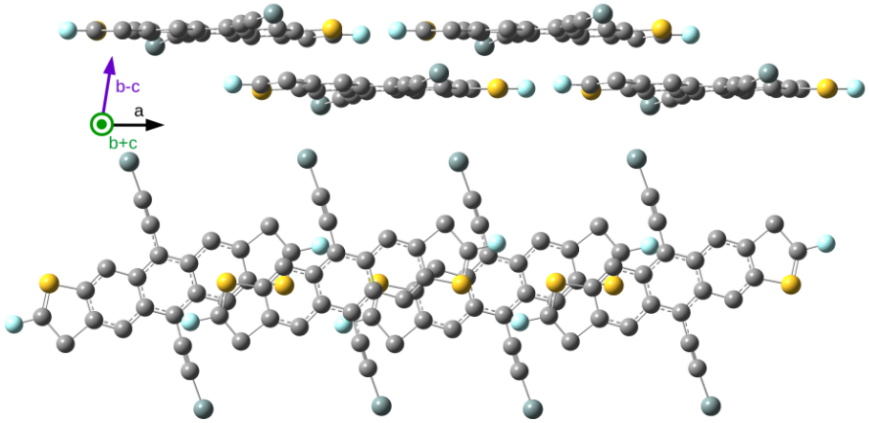

Figure 4

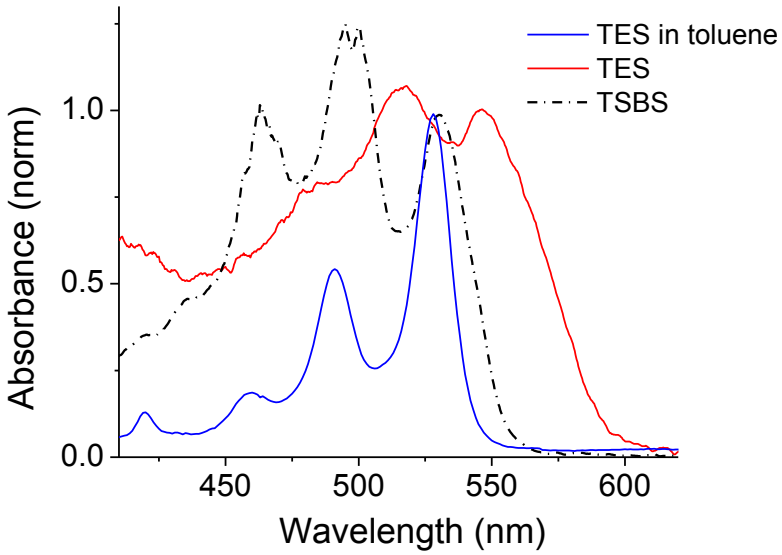
TES in toluene
TES
TSBS
Absorbance (norm)
1.0
0.5
0.0
450
500
550
600
Wavelength (nm)

Figure 5

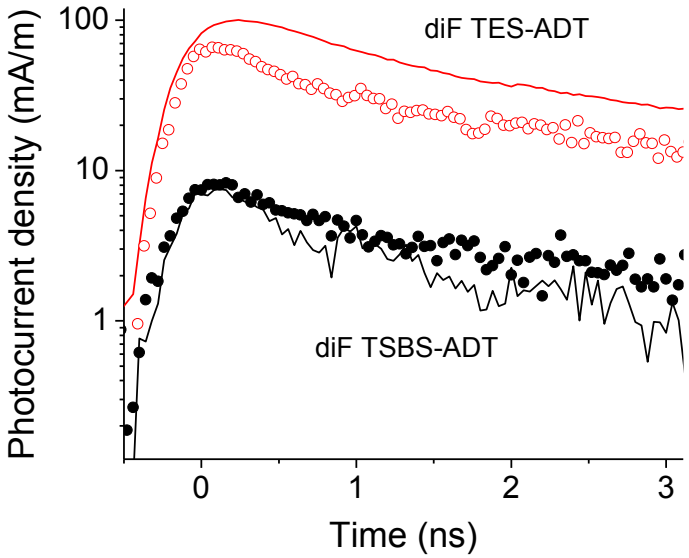
Photocurrent density (mA/m)
100
10
1
diF TES-ADT
diF TSBS-ADT
0
1
2
3
Time (ns)

Figure 6

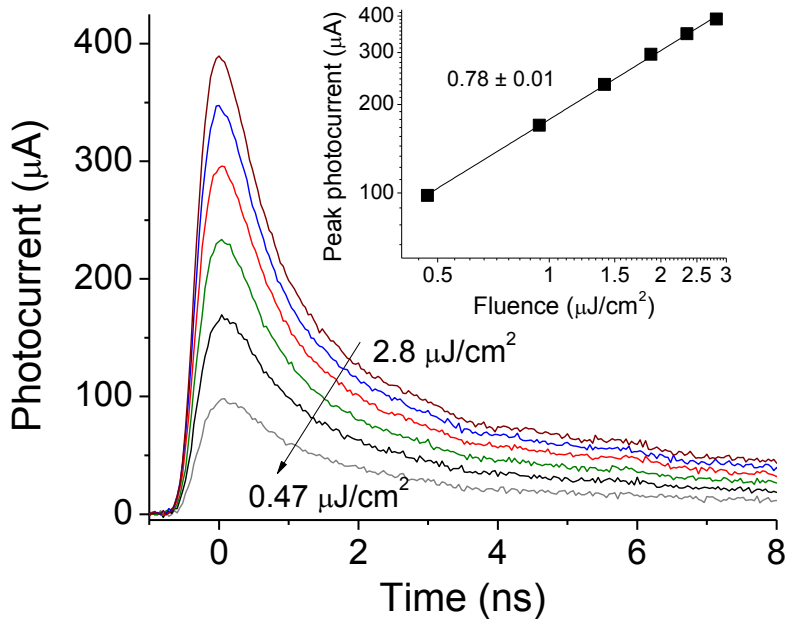
Photocurrent (μA)
Time (ns)
2.8 μJ/cm2
0.47 μJ/cm2
Peak photocurrent (μA)
Fluence (μJ/cm2)
0.78 ± 0.01

Figure 7

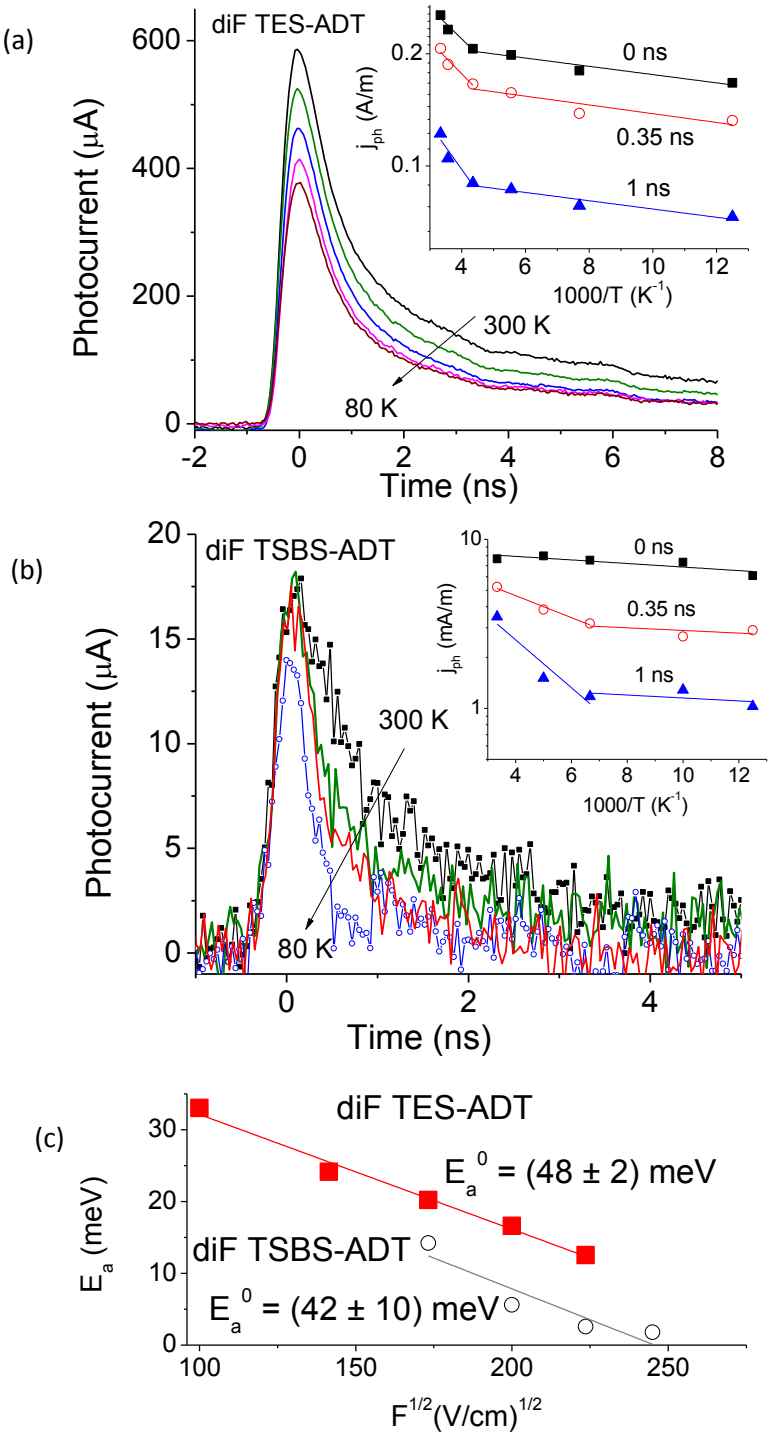
(a)
diF TES-ADT
Photocurrent (μA)
Time (ns)
0 ns
0.35 ns
1 ns
300 K
80 K
j_{ph} (A/m)
1000/T (K^{-1})
(b)
diF TSBS-ADT
Photocurrent (μA)
Time (ns)
0 ns
0.35 ns
1 ns
300 K
80 K
j_{ph} (mA/m)
1000/T (K^{-1})
(c)
diF TES-ADT
E_a^0 = (48 ± 2) meV
diF TSBS-ADT
E_a^0 = (42 ± 10) meV
E_a (meV)
$F^{1/2}(V/cm)^{1/2}$

Figure 8

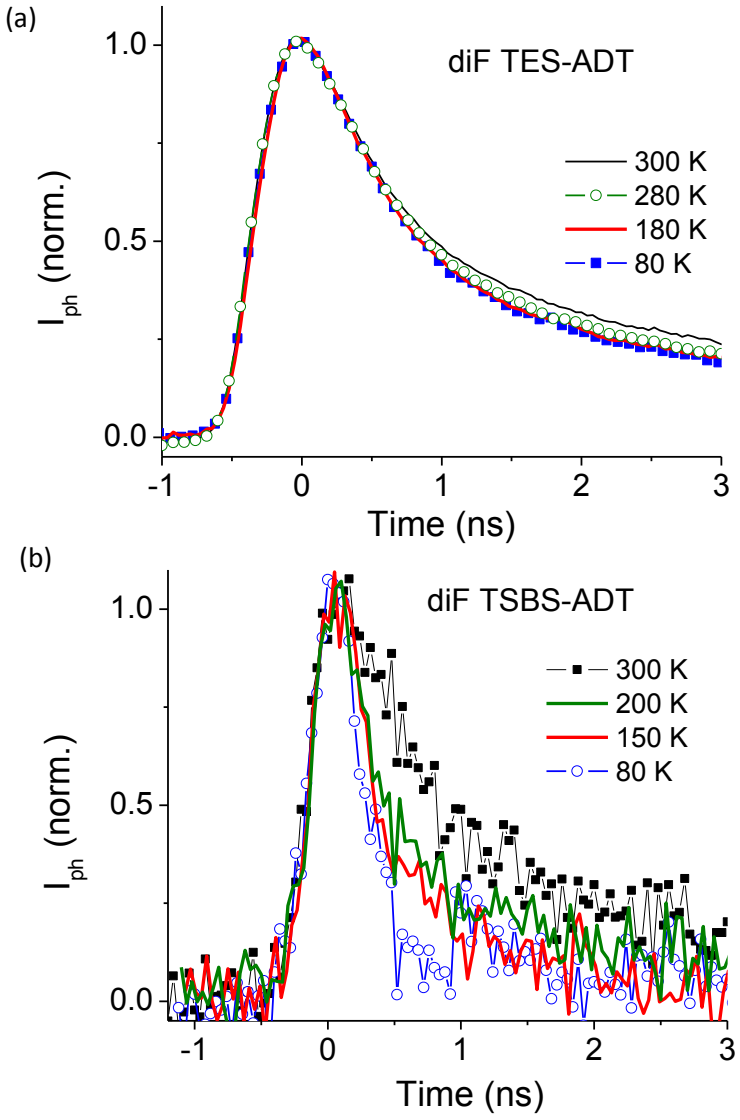
(a)
diF TES-ADT
300 K
280 K
180 K
80 K
I_{ph} (norm.)
Time (ns)
(b)
diF TSBS-ADT
300 K
200 K
150 K
80 K
I_{ph} (norm.)
Time (ns)

Figure 9

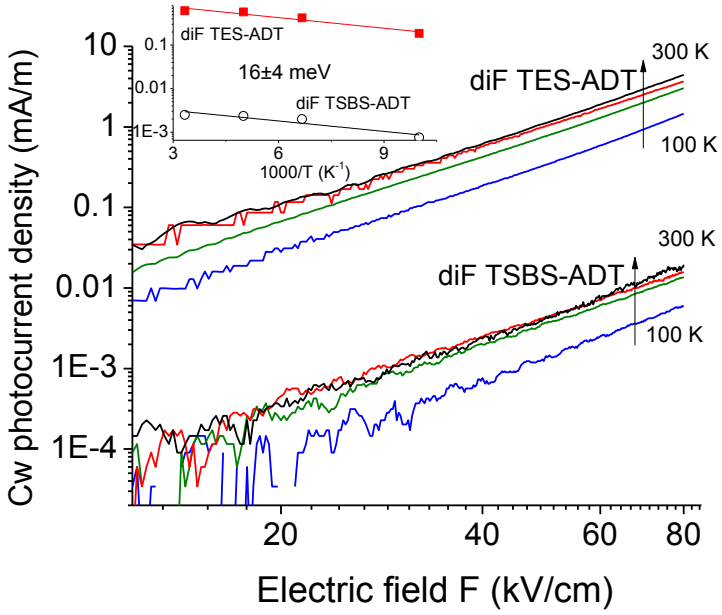
Cw photocurrent density (mA/m)
10
1
0.1
0.01
1E-3
1E-4
20
40
60
80
Electric field F (kV/cm)
diF TES-ADT
300 K
100 K
diF TSBS-ADT
300 K
100 K
0.1
0.01
1E-3
diF TES-ADT
16±4 meV
diF TSBS-ADT
3
6
9
1000/T (K-1)